A theoretical model for EM-ML reconstruction algorithms applied to rotating PET scanners

A theoretical model for EM-ML reconstruction algorithms applied to rotating PET scanners

A Iriarte[1], C O S Sorzano[2,3], J M Carazo[2], J L Rubio[4,5] and R Marabini[1]

[1] Escuela Politécnica Superior, Universidad Autónoma de Madrid, 28049 Madrid, Spain
[2] Centro Nacional de Biotecnología, Universidad Autónoma de Madrid, 28049 Madrid, Spain
[3] Bioengineering Laboratory, Universidad San Pablo CEU, 28668 Boadilla del Monte Madrid, Spain
[4] Biomedical Image Technologies Group, Dpto. Ingeniería Electrónica, ETSI Telecomunicación, Universidad Politécnica de Madrid, 28040 Madrid, Spain
[5] Networking Research Center on Bioengineering, Biomaterials and Nanomedicine (CIBER-BBN), Madrid, Spain

E-mail: ana@cnb.csic.es

Abstract

In this paper we show how to compute the normalizing and the system matrix terms of the EM-ML reconstruction algorithm for rotating planar detector PET scanners. The method introduced is valid for either pixelated or continuous scintillators. We base our computations in geometrical considerations, but other effects of the PET process can be easily included. In this regard, the intrinsic resolution of the detection system, the depth of interaction (DOI) of the incident gamma rays and the efficiency of the scintillators have been modeled in our development. The computation of the normalizing term and the system matrix is valid for any basis function used for the discrete approximation of the radionuclide concentration. We show that our computations are comparable to those of a Monte Carlo method at a small fraction of the computational cost.

1. Introduction

In the process of PET imaging, the step of image reconstruction (Lewitt and Matej 2003) is crucial for obtaining high-quality results, both qualitatively as well as quantitatively, for accurate diagnosis and posterior analysis and processing. Vardi *et al* (1985) introduced an algorithm based on expectation maximization and maximum likelihood (EM-ML) for three-dimensional reconstruction from PET data. Over the past 20 years, much of the work in statistically based algorithms has focused on finding alternative implementations of the EM-ML algorithm that converge faster or offer improved resolution, contrast and/or signal-to-noise ratio.

Nowadays, data are manipulated in a digital form. That is, algorithms that work with continuous magnitudes should be written so that they can handle digital images that represent the physical magnitude. There are many ways to represent a continuous image using a discrete set of numbers. A popular approach considers an image as being constructed by the sum of shifted copies of a volume element (a voxel, for example), usually called a basis function. The explicit consideration of continuous distributions for the reconstructed volume is in agreement with the recent appearance of continuous detectors (Giménez *et al* 2004, Staelens *et al* 2004, Tavernier *et al* 2005). The use of continuous scintillators instead of pixelated blocks allows us to improve both the spatial and energy resolution, while avoiding the problems of light collection efficiency that are related to fine pixelation of the crystals. Additionally, the cost and complexity of the detector are reduced. The use of LSO, with high scintillation efficiency as well as higher cross section for 511 keV gamma rays and faster decay time than NaI(T1), prevents the light from spreading too far in the crystal and results in excellent count-rate performance (Siegel *et al* 1995). The main disadvantages currently associated with the use of these kinds of scintillators are non-uniformity and nonlinearity in the camera response, but their effects can be minimized during the process of camera calibration (Sanchez *et al* 2004). The more accurate lines of response (LORs) provided by continuous scintillator cameras are naturally handled by list-mode versions of the EM-ML reconstruction algorithm (Rahmim *et al* 2005, Reader *et al* 1998, Reader *et al* 2002, Parra and Barrett 1998). List-mode reconstruction algorithms modify the EM-ML equations so that each LOR is considered individually instead of being grouped in discrete detector bins.

The key challenge of the EM-ML algorithm implementation is the calculation of the so-called system matrix and normalization terms (Ortuño *et al* 2004, Ortuño *et al* 2006, Scheins *et al* 2006), i.e., the probability that an emission from a given basis function is detected at a certain LOR and the probability that an emission from a given basis function is ever detected by the detector arrangement. For computing these probabilities, the geometry of the detectors has to be explicitly taken into account (Levkovtiz *et al* 2001, Phelps and Cherry 1998, Qi *et al* 1998) as well as other effects that take place in the PET process such as the intrinsic resolution and crystal thickness of the detectors (Staelens *et al* 2004) or the detection efficiency of the scintillators (Levkovtiz *et al* 2001).

In this paper, we introduce an analytical method to compute the system matrix and the normalization terms of the EM-ML list-mode algorithm for a rotating planar detector PET camera with either continuous or pixelated scintillators. Our method is able to compute these factors for any arbitrary basis function at a cost that is a small fraction of the computational cost of sophisticated Monte Carlo simulations. We show that the system matrix and the normalization factor computed by our method are similar to those computed by Monte Carlo simulations.

2. Background

The mathematical development of Vardi *et al* (1985) assumes that positron emissions occur according to a Poisson process in a certain region of $\mathbb{R}^3$ with an unknown intensity function $\lambda(\mathbf{r}) : \mathbf{r} \in \mathbb{R}^3$. Therefore, the measured data set $n^*(d)$ (the total number of coincidences in each tube d formed by a pair of detectors) constitutes also a Poisson random variable with a mean:

$$\lambda^*(d) = \int_{\mathbb{R}^3} \lambda(\mathbf{r}) c(\mathbf{r}, d) \, \mathrm{d}\mathbf{r}, \tag{1}$$

where $d = 1, \ldots, D$ (D being the maximum number of detector bins), and $c(\mathbf{r}, d)$ is the probability that a line originated at a spatial point $\mathbf{r}$ is detected at the discrete tube d. When

implementing the reconstruction algorithm described in Vardi *et al* (1985), it was assumed that a fine grid of B basis functions exists such that if $v(\mathbf{r} - \mathbf{r}_b)$ stands for the general mathematical expression of the basis function centered in the point $\mathbf{r}_b$ and $\lambda(b)$ is the weight of the bth basis function, then

$$\lambda^*(d) \approx \sum_{b=1}^{B} \lambda(b) p(b, d), \tag{2}$$

where

$$p(b, d) = \int_{\mathbb{R}^3} v(\mathbf{r} - \mathbf{r}_b) c(\mathbf{r}, d) \, d\mathbf{r}, \tag{3}$$

$p(b, d)$ is the probability that an event generated in the region defined by the bth function is detected in the tube d. Coefficients $p(b, d)$ can be arranged in a matrix called the system matrix.

At this point, the activity distribution $\lambda(\mathbf{r})$ that maximizes the probability of obtaining the measured data $n^*(d)$ must be found. Since the collected data follow a Poisson model, this corresponds to the maximization of the probability function:

$$P(n^*) = \prod_{d=1}^{D} e^{-\lambda^*(d)} \frac{\lambda^*(d)^{n^*(d)}}{n^*(d)!}. \tag{4}$$

The maximization of the expression in (4) can be satisfied with many iterative schemes. Particularly appealing is that given by the expectation maximization algorithm. The final expression given in Vardi *et al* (1985) is an instance of this algorithm:

$$\lambda^{\text{new}}(b) = \frac{\lambda^{\text{old}}(b)}{p(b)} \sum_{d=1}^{D} \frac{n^*(d) p(b, d)}{\sum_{b=1}^{B} \lambda^{\text{old}}(b) \, p(b, d)}, \qquad \text{where} \quad 0 < p(b) = \sum_{d=1}^{D} p(b, d) \leqslant 1. \tag{5}$$

The term $p(b)$ is a normalization factor representing the probability of detecting a pair of photons arbitrarily emitted from within the function b (considering all possible detectors).

There is a growing trend to use PET measurements in the so-called list-mode data. The list-mode data are a list of coincident gamma pairs that are serially stored in the chronological order of their registration. This mode has the advantage of a higher accuracy since photons need not be discretized into sinograms. Reader *et al* (1998) and Parra and Barrett (1998) developed an expression equivalent to (5) for the case of data sorted in the list mode:

$$\lambda^{\text{new}}(b) = \frac{\lambda^{\text{old}}(b)}{p(b)} \sum_{n=1}^{N} \frac{p(b, d_n)}{\sum_{b=1}^{B} \lambda^{\text{old}}(b) \, p(b, d_n)}, \tag{6}$$

where N is the total number of measured events. As can be seen, each line is treated individually instead of being grouped into tubes of response, and thus the measurement term $n^*(d)$ is now equal to one in the numerator of the summation. Moreover, for the list-mode case, the terms $p(b, d_n)$ of the system matrix stand for the probability that an emission from the basis function b is detected along the LOR d defined by the nth event. The list-mode reconstruction equation is especially suited for PET systems that make use of continuous detectors, since in these systems events are not binned into discrete detectors.

3. The system matrix and normalization term for an arbitrary basis function

As can be inferred from (5) and (6), the implementation of the EM-ML algorithm implies mainly the implementation of two sets of terms, namely $p(b)$ (normalizing term) and $p(b, d)$

(system matrix). In the following, we introduce an analytical method to compute the normalizing term and the system matrix for any basis function in the field of view (FOV) of scanners with rotating planar detectors (see figure 1), either continuous or pixelated. We perform these calculations in two steps. First, we compute the normalizing term and the system matrix for a single emitting point in the FOV. Sections 3.1 and 3.2 describe the fundamentals of the methodology proposed for these calculations. Second, in section 3.3 we extend the results obtained for a single emitting point to the general case of any basis function.

3.1. Computation of the normalizing term for a single emitting point

The normalizing term for a single emitting point in the FOV of a PET scanner is the probability that a pair of gamma photons emitted from that point is detected by the scanner. The normalizing term has been traditionally computed as shown in (5), making use of the discrete nature of the pixelated detectors. With the increasing number of crystals in modern tomographs, the calculation of the individual probabilities of detection over all possible system tubes poses a challenge from the computational cost point of view. This can be a limiting factor, especially in an environment of design and evaluation of PET cameras, where sensitivity calculations play a major role. Moreover, in the case of continuous detectors, no segmentation in tubes exists, and therefore the summation in (5) must be correctly expressed as an integral. These objections evidence the need of an analytical method to compute the normalizing term. There already exist a few analytical calculations of this term (Reader *et al* 1998, Levkovtiz *et al* 2001, Soares *et al* 2003); however, in all of these developments there exists a compression of the two transaxial spatial variables into a radial variable (i.e. cylindrical symmetry is assumed). A detailed discussion of the experimental importance of this factor is given in section 4.1.1. The following analytical development does not assume cylindrical symmetry and is independent of the continuous/pixelated nature of the scintillators.

Consider the basic scanner consisting of just two parallel planar detector heads whose dimensions and coordinate axes are shown in figure 1. Let φ and γ be the polar and azimuthal angles, respectively. If we assume a uniform distribution of the emissions over the sphere (i.e. the joint probability density function of φ and γ is $f(\varphi, \gamma) = \cos\varphi/2\pi$), the probability that an emission from a point $\mathbf{r}_0$ of coordinates (x_0, y_0, z_0) in any plane Π_γ parallel to the z-axis (see figure 1) intersects both of the planar detector heads can be computed as

$$p(\mathbf{r}_0, \Pi_\gamma) = \int_{\alpha_\varphi(\mathbf{r}_0, \gamma)}^{\beta_\varphi(\mathbf{r}_0, \gamma)} \frac{1}{2\pi} \cos\varphi \, \mathrm{d}\varphi. \tag{7}$$

As can be observed in figure 1, the integration limits $\alpha_\varphi(\mathbf{r}_0, \gamma)$ and $\beta_\varphi(\mathbf{r}_0, \gamma)$ are the maximum detectable angles from $\mathbf{r}_0$ within the plane Π_γ. Closed-form expressions for $\alpha_\varphi(\mathbf{r}_0, \gamma)$ and $\beta_\varphi(\mathbf{r}_0, \gamma)$ are given in appendix A.1.

Even if a photon intersects a detector it may not interact with it. The detection efficiency of the scintillator material, quantified through its physical attenuation constant, μ_0, must be considered. The probability of detecting a pair of gamma photons that intersect the left and right detectors with lengths $L_1(\mathbf{r}_0, \varphi, \gamma)$ and $L_2(\mathbf{r}_0, \varphi, \gamma)$ respectively can be approximated by

$$p(\mathbf{r}_0, \varphi, \gamma) = (1 - \mathrm{e}^{-\mu_0 L_1(\mathbf{r}_0, \varphi, \gamma)})(1 - \mathrm{e}^{-\mu_0 L_2(\mathbf{r}_0, \varphi, \gamma)}). \tag{8}$$

The probability of detecting an emission from a point $\mathbf{r}_0$ in any plane Π_γ is

$$p(\mathbf{r}_0, \Pi_\gamma) = \int_{\alpha_\varphi(\mathbf{r}_0, \gamma)}^{\beta_\varphi(\mathbf{r}_0, \gamma)} \frac{\cos\varphi}{2\pi} p(\mathbf{r}_0, \varphi, \gamma) \, \mathrm{d}\varphi.$$

$$x - x_0 = \tan \gamma \, (y - y_0)$$
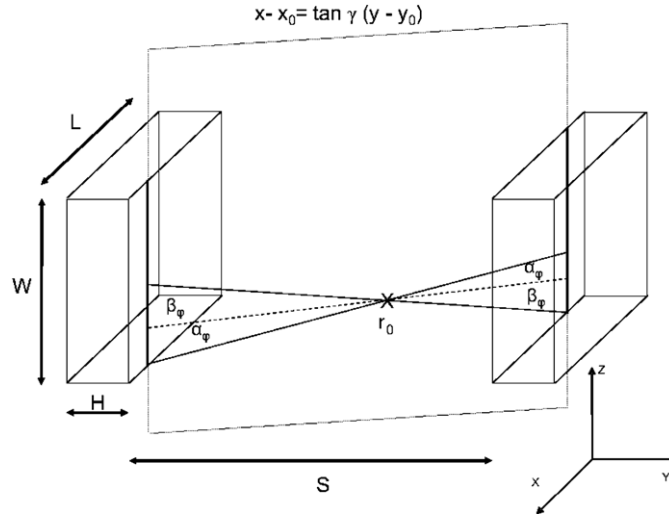
Figure 1. Geometrical characterization of the range of detectable emissions from the point $\mathbf{r}_0$ within the plane Π_γ. γ is the angle formed by the plane parallel to the z-axis Π_γ and the plane $x = x_0$. The angles $\alpha_\varphi(\mathbf{r}_0, \gamma)$ and $\beta_\varphi(\mathbf{r}_0, \gamma)$ define the maximum and minimum φ detectable LORs within the plane Π_γ. The dashed line is the intersection of $z = z_0$ and Π_γ planes. The reference axes used through this work are supposed to be centered with respect to the planar detectors but for space reasons are shown at the lower right corner of the figure.

The expression for the probability of detection of any pair of photons emitted from $\mathbf{r}_0$ in the case of the basic two parallel detector heads is then

$$p(\mathbf{r}_0) = \int_{\alpha_\gamma(\mathbf{r}_0)}^{\beta_\gamma(\mathbf{r}_0)} p(\mathbf{r}_0, \Pi_\gamma) \, d\gamma. \tag{9}$$

The range of detectable planes is defined again by the angle seen by the point $\mathbf{r}_0$ into the detector heads, now in the xy plane, as shown in figure 2. Appendix A.2 provides analytical expressions for the angular limits $\alpha_\gamma(\mathbf{r}_0)$ and $\beta_\gamma(\mathbf{r}_0)$.

Let us consider now the general case of a dual-head camera in which the detector heads in figure 1 rotate at discrete steps of ψ degrees around the z-axis. If the couple of detector heads has N possible angular positions, let us call $p(\mathbf{r}_0, \mathrm{step}_i)$ the probability of detection of a pair of photons emitted from $\mathbf{r}_0$ by the detector heads in position i $(i = 0, \ldots, N - 1)$. The values of $p(\mathbf{r}_0, \mathrm{step}_i)$ can be computed easily from the expressions developed above for the unrotated case just by rotating the emitting point by $-i\psi$ degrees and leaving detector heads on their initial positions. The probability of detecting anything emitted from $\mathbf{r}_0$ in this scanner is

$$p(\mathbf{r}_0) = \sum_{i=0}^{N-1} p(\mathbf{r}_0, \mathrm{step}_i) p(\mathrm{step}_i), \tag{10}$$

where $p(\mathrm{step}_i)$ is the probability that the dual head is situated at the ith angular position. For the camera described above, the detector heads spend the same amount of time in each position and therefore

$$p(\mathrm{step}_i) = \frac{1}{N}. \tag{11}$$
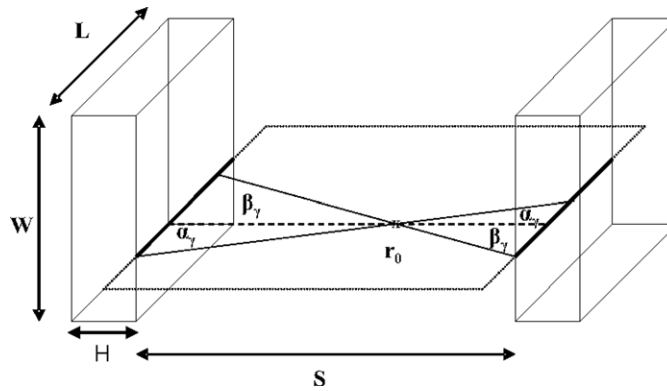
Figure 2. Geometrical characterization of the range of detectable emissions from the point $\mathbf{r}_0$ within the plane xy. The angles $\alpha_\gamma(\mathbf{r}_0)$ and $\beta_\gamma(\mathbf{r}_0)$ define the maximum and minimum γ detectable LORs within the plane xy.

It should be remarked that the expression in (10) is a function of the three spatial coordinates (x_0, y_0, z_0) of $\mathbf{r}_0$. No cylindrical symmetry has been assumed in the transaxial planes. The importance of this fact can be observed in section 4.1.1, where the probability of detection along different circumferences in the plane xy is calculated for the case of commercially available PET systems showing that there can be fluctuations up to 300% in the probability of detection of points located at the same radial distance. This result clearly invalidates the cylindrical symmetry assumption.

3.2. Computation of the system matrix for a single emitting point.

As mentioned at the beginning of this section, the terms $p(b, d)$ stand for the probability that an emission from the region within the basis function b is detected in a tube d defined by a pair of pixelated detectors. If continuous detectors are used, then the detector tube reduces to a single line. Traditionally, the system matrix has been computed either by means of Monte Carlo simulations or as the intersection of the basis function b with the event defined by d. The former approximation has the drawback of being computationally expensive whereas the latter is based on a too simplified model of the PET process.

Staelens *et al* (2004) introduced an analytical method (on which the presented development is based) for computing the system matrix for a single emitting point that takes into account the spatial intrinsic resolution during data formation. Due to this effect, the localization of events in the detector heads is not perfectly defined and, therefore, spatial uncertainty exists for the detected LORs. In section 3.2.1, it is shown how this uncertainty can be modeled through a probability density function of the measured position d_{LOR} centered at the actual position of interaction in the detector head, d'_{LOR}. As in Staelens *et al* (2004) we model this function by a bidimensional Gaussian distribution, whose parameters are accurately defined in section 3.2.2. Then, the likelihood of detecting an emission from $\mathbf{r}_0$ in d_{LOR} is calculated. In order to include the intrinsic resolution effect in our model, this likelihood is achieved by integrating, over every d'_{LOR} emitted by $\mathbf{r}_0$ in a neighborhood of d_{LOR}, the likelihood of detecting d'_{LOR} in d_{LOR} (given by the Gaussian density function). Finally, the probability of detection of $\mathbf{r}_0$ in d required by the EM-ML algorithm must be calculated by integrating its
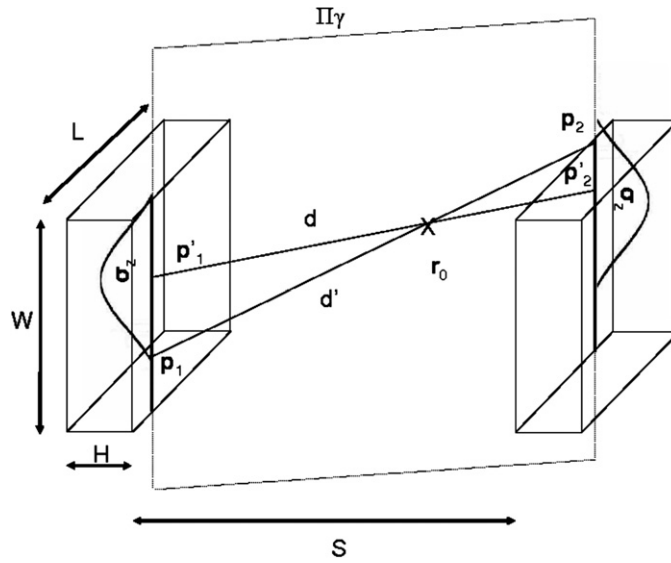
Figure 3. Geometrical representation of the uncertainty of detection along the axial direction. The plane Π_γ is the plane parallel to the Z-axis containing d and d'.

likelihood over the limits that define the event d in the (continuous or pixelated) detector heads. Section 3.2.3 shows how to perform these integrals.

Some modifications have been introduced with respect to the work by Staelens *et al* (2004). First, as can be seen in section 3.2.1 we have replaced the uniform model for the probability of detection along the photon path by an exponential model. The exponential model, based on Lambert's absorption law, constitutes a more accurate approximation for the probability of interaction of gamma rays in matter. Second, as shown in section 3.2.2, we have introduced a dependence of the Gaussian standard deviation σ with the depth of the first interaction of the gamma ray with the crystal. This dependence is based on the fact that an increase in detector thickness causes an increase in the positioning error (Stickel and Cherry 2005). Finally, we have added the term for the joint probability density function of γ and φ (the angles that define each emitted line) in order to make the distribution of emissions uniform over the sphere (see section 3.2.3)).

3.2.1. Uncertainty model. In this section, a model for the likelihood that a pair of photons interacting at given positions leads to detection in another location will be introduced. The LOR, d_{LOR}, in which the pair of photons has been detected can be defined by two points $\mathbf{p}_1 = (x_1, y_1, z_1)$ and $\mathbf{p}_2 = (x_2, y_2, z_2)$ on the internal surfaces of the detector head. Let us first assume that the LOR d'_{LOR} at which the event actually took place is contained in the plane Π_γ (see figure 3). We denote the endpoints of this LOR by $\mathbf{p}'_1 = (x_1, y_1, z'_1)$ and $\mathbf{p}'_2 = (x_2, y_2, z'_2)$. These are the intersection points of the LOR (defined by $\mathbf{r}_0$ and the angles φ and γ) with the internal surfaces of the detectors. Let us also assume that the probability of detecting an event at d_{LOR} when it actually occurred at d'_{LOR} follows a Gaussian distribution with zero mean and standard deviation σ_z (see figure 3). Then, the likelihood of detecting the photons at d_{LOR} knowing that the interaction actually occurred at d'_{LOR} can be computed as

$$f(d_{\mathrm{LOR}}|d'_{\mathrm{LOR}}) = f(\mathbf{p}_1|\mathbf{p}'_1)f(\mathbf{p}_2|\mathbf{p}'_2) = \frac{1}{2\pi\sigma_z^2}\, \mathrm{e}^{-\frac{1}{2\sigma_z^2}(z_1-z'_1(\mathbf{r}_0,\varphi))^2}\, \mathrm{e}^{-\frac{1}{2\sigma_z^2}(z_2-z'_2(\mathbf{r}_0,\varphi))^2}. \tag{12}$$
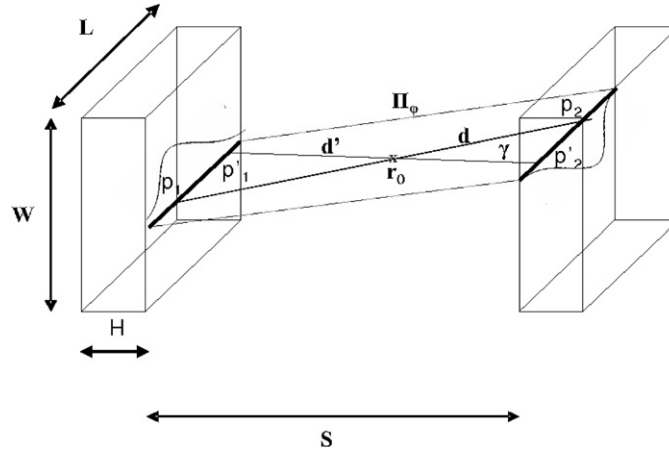
Figure 4. Geometrical representation of the uncertainty of detection along the tangential direction when this matches the *X*-axis. The plane Π_φ is the plane containing d and d'.

Equation (12) models uncertainty just in the axial direction, which always fits the *z*-axis of the scanner. For the case of uncertainty in the tangential coordinate of detection, the uncertainty direction does not match with any of the reference axes shown in figure 1, but changes with the rotation of the setup around the *z*-axis. Nevertheless, just by applying the appropriate rotation, the results for the case of matching with the *x*-axis (figure 4 shows this uncertainty situation) applies to any arbitrary case. Therefore, by simple combination of the axial and tangential cases we can obtain a general result for the detection uncertainty in both directions:

$$
f(d_{\text{LOR}}|d'_{\text{LOR}}) = \frac{1}{2\pi\sigma_z^2}\, e^{-\frac{1}{2\sigma_z^2}(z_1 - z'_1(\mathbf{r}_0,\varphi))^2}\, e^{-\frac{1}{2\sigma_z^2}(z_2 - z'_2(\mathbf{r}_0,\varphi))^2}
$$
$$
\frac{1}{2\pi\sigma_x^2}\, e^{-\frac{1}{2\sigma_x^2}(x_1 - x'_1(\mathbf{r}_0,\gamma))^2}\, e^{-\frac{1}{2\sigma_x^2}(x_2 - x'_2(\mathbf{r}_0,\gamma))^2}. \tag{13}
$$

Closed expressions for $x'_1(\mathbf{r}_0,\gamma)$, $x'_2(\mathbf{r}_0,\gamma)$, $z'_1(\mathbf{r}_0,\varphi)$ and $z'_2(\mathbf{r}_0,\varphi)$ can be found in appendix A.3.

When dealing with oblique incidences on thicker crystals the depth of interaction (DOI) of the photons also contributes to the detection uncertainty, as shown in figure 5. The coordinates x'_1, x'_2 and z'_1, z'_2 of d'_{LOR} (and therefore the likelihood of detecting an emission at d_{LOR} when it actually took place at d'_{LOR}, given by (13)) depend on the depths at which the photons are detected on the crystal head. The uncertainty of detection when the DOI of the incident photons is taken into account can be computed by integrating the Gaussian uncertainty given by (13) over every possible depth weighted by the corresponding probability of interaction at that depth:

$$
f(d_{\text{LOR}}|d'_{\text{LOR}})_{\text{DOI}} = \frac{1}{2\pi\sigma_x\sigma_z}\int_0^{L_1(\mathbf{r}_0,\varphi,\gamma)} e^{w_1(\mathbf{r}_0,\varphi,\gamma,l_1)} f(l_1)\, dl_1
$$
$$
\frac{1}{2\pi\sigma_x\sigma_z}\int_0^{L_2(\mathbf{r}_0,\varphi,\gamma)} e^{w_2(\mathbf{r}_0,\varphi,\gamma,l_1)} f(l_2)\, dl_2 \tag{14}
$$
$$
w_i(\mathbf{r}_0,\varphi,\gamma,l_i) = -\left\{ \frac{[z_i - z'_i(\mathbf{r}_0,\varphi,l_i)]^2}{2\sigma_z^2} + \frac{[x_i - x'_i(\mathbf{r}_0,\gamma,l_i)]^2}{2\sigma_x^2} \right\}, \quad i = 1, 2.
$$
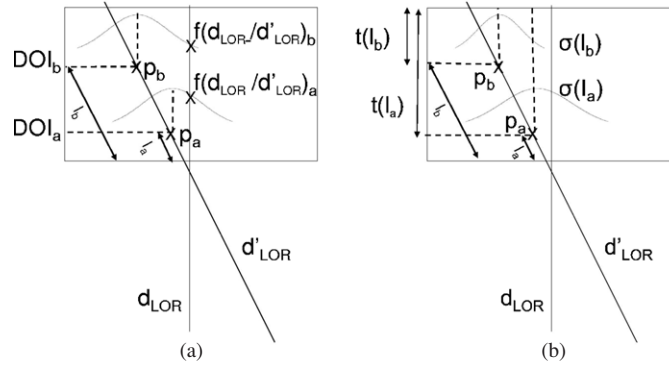
Figure 5. (a) Effect of the depth of interaction (DOI) on the detection uncertainty. The depth l_i at which the photon actually interacts with the detector head defines the position of the Gaussian density function that gives the probability of detecting d'_{LOR} in d_{LOR}, $f(d/d')_i$. (b) Dependence of the spatial resolution with the DOI of the first interaction of the gamma photon on the scintillator. If the first interaction takes place at p_a, the error positioning is bigger than if it occurs at p_b as the crystal width the photon 'sees' is thicker at p_a than at p_b. Therefore the standard deviation of the Gaussian that models detection uncertainty should be bigger at p_a than at p_b: $\sigma_a > \sigma_b$.

The integration variable l_i, $i = 1, 2$, is the depth at which the photons enter each detector (right or left) in the direction of d'_{LOR} (given by φ and γ), L_1 and L_2 are the intersection lengths of d'_{LOR} with the detector heads, and $f(l)$ stands for the probability that the first interaction of the photon occurs at that depth. We model the detection probability of 511 keV photons through an exponential approximation:

$$f(l) = \mu_0\, e^{-\mu_0 l}. \tag{15}$$

As has been mentioned, this exponential model represents a more accurate approximation than the uniformity assumption made by Staelens *et al* (2004) for the most currently used scintillation materials. The integration of this probability density function over the intersection length of the photon across the detector leads, as expected, to the expression for the detection probability of the photon across the crystal given by (8).

3.2.2. Gaussian characterization. In this section, we provide a characterization of the Gaussian distribution that models the likelihood of detecting d'_{LOR} in d_{LOR}. Our model takes into account the influence of the DOI of the interacting photons on the final event positioning. The two main interactions that a 511 keV photon can undergo in detector materials are Compton scattering and photoelectric absorption. A Compton scattering interaction results in a scattered photon and a recoil electron. Photoelectron absorption results in a photoelectron and in a characteristic x-ray. The x-ray produced in photoelectric absorption and the Compton scattered photon may interact again at some distance from the original interaction site or alternatively they may escape from the detector. Therefore, each 511 keV gamma photon emitted can cause interactions at different points in the scintillator crystal. The position of the final event depends on the particular detector readout and signal processing of the system. Independently of the positioning method, the increase in the number of interactions in the scintillator leads to an increase in the error of the location of the initial photon interaction. As Stickel and Cherry (2005) show, the number of events that undergo multiple interactions (and therefore the degradation of the spatial resolution) increases with detector thickness. Based on this relationship between the crystal thickness and the positioning error, we propose a model

in which the detection uncertainty changes with the DOI of the first interaction of the photon in the crystal (the integrating variable l in (14)). From the above statements it follows that the uncertainty should be maximum for the interactions occurring at $l = 0$ and that it will decrease as the photon interacts more deeply. The parameter that quantifies the uncertainty in the detection is the standard deviation (σ_x and σ_z) of the Gaussian probability distribution. Therefore, we have chosen to decrease the value of σ with the value of the crystal thickness the gamma photon 'sees' after its first interaction (in the following $t(l)$). Based on the experiments that will be shown in section 4.2, this dependence has been approximated by a linear function:

$$\sigma(l) = mt(l) + b, i = z, x. \tag{16}$$

Without loss of generality, it has been assumed that the uncertainty model in the z- and x-coordinates is the same. As has been mentioned, $t(l)$ stands for the crystal thickness that remains for the gamma photon after its first interaction with the detector (see figure 5(b)). Appendix A.4 explains how to compute the value of this parameter. The values of the parameters m and b depend on the particular resolution features of the scanner being considered. As shown in Stickel and Cherry (2005), the main sources of resolution loss are the positron physics, the detector design, and the readout and signal processing of the particular scanner. Therefore, in order to obtain an accurate estimation of the intrinsic resolution, the parameters m and b should be obtained experimentally from the scanner for which the system matrix has to be computed. The available Monte Carlo simulators still do not provide the tools to faithfully reproduce many of the current positioning methods (Tavernier *et al* (2005) shows some of these complex algorithms for position determination). Section 4.2 provides an experimental methodology to obtain the linear parameters m and b.

This l-dependent uncertainty model can be easily included in the previous model for the likelihood that an emission in d'_{LOR} leads to d_{LOR} just by substituting in (14) the fixed σ by the l-coordinate-dependent value. The final expression for the probability density function $f(d_{\text{LOR}}|d'_{\text{LOR}})_{\text{DOI}}$ is

$$
f(d_{\text{LOR}}|d'_{\text{LOR}})_{\text{DOI}} = \int_0^{L_1(\mathbf{r}_0, \varphi, \gamma)} \frac{1}{2\pi \sigma(l_1)^2} \, e^{w_1(\mathbf{r}_0, \varphi, \gamma, l_1)} f(l_1) \, dl_1
$$

$$
\int_0^{L_2(\mathbf{r}_0, \varphi, \gamma)} \frac{1}{2\pi \sigma(l_2)^2} \, e^{w_2(\mathbf{r}_0, \varphi, \gamma, l_2)} f(l_2) \, dl_2 \tag{17}
$$

$$
w_i(\mathbf{r}_0, \varphi, \gamma, l_i) = -\left\{ \frac{[z_i - z'_i(\mathbf{r}_0, \varphi, l_i))]^2}{2\sigma_z(l_i)^2} + \frac{[x_i - x'_i(\mathbf{r}_0, \gamma, l_i)]^2}{2\sigma_x(l_i)^2} \right\} \quad i = 1, 2.
$$

3.2.3. Integration. In this section, we provide expressions for the system matrix terms based on the integration of the results obtained in sections 3.2.1 and 3.2.2. First, the likelihood that an emission from $\mathbf{r}_0$ leads to an event detected in d_{LOR} must be computed by integrating (17) over every d'_{LOR} that intersects the detectors:

$$
f(\mathbf{r}_0, d_{\text{LOR}}) = \int_{\alpha_\gamma(3\sigma_H, L)}^{\beta_\gamma(3\sigma_H, L)} \int_{\alpha_\varphi(3\sigma_H, W)}^{\beta_\varphi(3\sigma_H, W)} f(d_{\text{LOR}}|d'_{\text{LOR}})_{\text{DOI}} \frac{\cos \varphi}{2\pi} \, d\varphi \, d\gamma. \tag{18}
$$

Each d'_{LOR} emitted from $\mathbf{r}_0$ has been characterized by the angles φ and γ. As has been mentioned, the inclusion of the term for the joint probability function of these angles ($\cos \varphi / 2\pi$) is one of the features that distinguish our development from previous ones. When implementing the integral in (18) numerically, the integration limits can be approximated to those including just the LORs d'_{LOR} whose intersection points in the crystal are in a neighborhood of d_{LOR} intersection points. This neighborhood has been chosen to be limited by the minimum of three times the maximum standard deviation σ_H (given by the evaluation

of (16) in $th(l = 0) = H$) and the detector limits. Closed-form expressions for the integration limits are given in appendix A.5.

Once the likelihood that an event originated at $\mathbf{r}_0$ is detected in d_{LOR} has been calculated in (18), the second step is to compute the system matrix terms for an emitting point $\mathbf{r}_0$. From this point on, our development makes a distinction between pixelated and continuous crystals (results until here apply to both cases). For the case of pixelated scintillators, the terms $p(\mathbf{r}_0, d)$ stand for the probability that an emission from $\mathbf{r}_0$ is detected in a tube d_{tube}, defined by a pair of pixelated detectors. These system matrix terms (in the following $p(\mathbf{r}_0, d_{tube})$) can be computed by integrating (18) over every possible LOR defined within the tube d_{tube}:

$$p(\mathbf{r_0}, d_{tube}) = \int_{S_{TUBE_1}} \int_{S_{TUBE_2}} f(\mathbf{r}_0, d_{LOR}) \, ds_1 \, ds_2$$
$$= \int_{C_{1x}} \int_{C_{1z}} \int_{C_{2x}} \int_{C_{2z}} f(\mathbf{r}_0, d_{LOR}(x_1, z_1, x_2, z_2)) \, dx_1 \, dz_1 \, dx_2 \, dz_2, \quad (19)$$

where S_{TUBE_1} and S_{TUBE_2} define the surfaces of the pixelated detectors in each (left or right) detector head. In this case, each line d_{LOR} has been parametrized by its intersection points $\mathbf{p_1}(x_1, y_1, z_1)$ and $\mathbf{p_2}(x_2, y_2, z_2)$ on the internal surfaces of the detector heads. In order to cover every pair of points $\mathbf{p_1}$ and $\mathbf{p_2}$ within the limits imposed by the pair of pixelated detectors that define d_{tube}, the integration limits are defined by the intervals:

$$C_{1x} = [C_{1xl}, C_{1xh}] = l[x_{1c} - C/2, x_{1c} + C/2] \quad (20a)$$

$$C_{1z} = [C_{1zl}, C_{1zh}] = [z_{1c} - C/2, z_{1c} + C/2] \quad (20b)$$

$$C_{2x} = [C_{2xl}, C_{2xh}] = [x_{2c} - C/2, x_{2c} + C/2] \quad (20c)$$

$$C_{2z} = [C_{2zl}, C_{2zh}] = [z_{2c} - C/2, z_{2c} + C/2], \quad (20d)$$

where (x_{c1}, y_{c1}, z_{c1}) and (x_{c2}, y_{c2}, z_{c2}) are the coordinates of the crystal centers and C is the crystal size. The subscript l is used to define the lower limit and the subscript h for the upper limit of the integral.

If continuous detectors are used, then the detector tube d_{tube} reduces to a single line, which in the list-mode EM-ML is defined by the nth event d_n. When integrating (18) for the computation of the system matrix for continuous scintillators, the integration limits must be those imposed by the resolution of the detection system, which measures how closely the line d_n can be resolved. For the case of pixelated scintillators, the resolution limits are imposed by the size of the pixelated crystals because the measured LOR positions are approximated by the center of the crystals where the pairs of photons were detected. However, for the case of continuous scintillators, no artificial grouping of the LORs within a region into a single detection exists, and thus the resolution limits are those imposed by the intrinsic resolution of the detecting system. Due to the Gaussian nature of the positioning error an appropriate measure of the spatial resolution is the full width at half maximum (FWHM $= 2.35\sigma$) of the wider of the Gaussian distributions that model the uncertainty (given by the evaluation of (16) in $th(l = 0) = H$) in (16)). The expression that computes the system matrix terms for the case of continuous detectors (in the following $p(\mathbf{r}_0, d_n)$) is given by

$$p(\mathbf{r_0}, d_n) = \int_{S_{FWHM_1}} \int_{S_{FWHM_2}} f(\mathbf{r}_0, d_{LOR} \, ds_1 \, ds_2$$
$$= \int_{C_{1x}} \int_{C_{1z}} \int_{C_{2x}} \int_{C_{2z}} f(\mathbf{r}_0, d_{LOR}(x_1, z_1, x_2, z_2)) \, dx_1 \, dz_1 \, dx_2 \, dz_2, \quad (21)$$

where S_{FWHM_1} and S_{FWHM_2} define the surfaces imposed by the Gaussian resolution limits in each detector head and therefore

$$C_{1x} = [C_{1xl}, C_{1xh}] = [x_{1c} - \text{FWHM}/2, x_{1c} + \text{FWHM}/2] \tag{22a}$$

$$C_{1z} = [C_{1zl}, C_{1zh}] = [z_{1c} - \text{FWHM}/2, z_{1c} + \text{FWHM}/2] \tag{22b}$$

$$C_{2x} = [C_{2xl}, C_{2xh}] = [x_{2c} - \text{FWHM}/2, x_{2c} + \text{FWHM}/2] \tag{22c}$$

$$C_{2z} = [C_{2zl}, C_{2zh}] = [z_{2c} - \text{FWHM}/2, z_{2c} + \text{FWHM}/2]. \tag{22d}$$

Note that (22) requires to integrate both in S_{FWHM_1} and S_{FWHM_2}. A single integration will provide the probability of detecting an emission produced in $\mathbf{r}_0$ in S_{FWHM_1}, but leaving undetermined the position of the second detection. Appendix A.6 shows a thorough development of (19) and (21) as a function of the expressions given by (18) and (17).

3.3. Generalization to arbitrary non-negative basis functions

It is necessary to extend the results for an emitting point $\mathbf{r}_0$ proposed in sections 3.1 and 3.2 to the general case of emissions from a basis function b. Let us interpret the basis function $v(\mathbf{r} - \mathbf{r}_b)$ centered at the position $\mathbf{r}_b$ as the probability density function of emitting points within a certain region of space (for this it is necessary that the basis function is non-negative and that it integrates to 1). Then, the probability of emitting a pair of photons within the region defined by the basis function b and the likelihood that these pairs of photons are detected by our detector head is

$$p(b) = \int_{\mathbb{R}^3} p(\mathbf{r}) v(\mathbf{r} - \mathbf{r}_b) \, \mathrm{d}\mathbf{r}. \tag{23}$$

Similarly, an expression can be obtained for the terms of the system matrix for any basis function based on the results for an emitting point:

$$p(b, d) = \int_{\mathbb{R}^3} p(\mathbf{r}, d) v(\mathbf{r} - \mathbf{r}_b) \, \mathrm{d}\mathbf{r}. \tag{24}$$

As has been already mentioned the terms $p(b, d)$ have traditionally been computed analytically by estimating the intersection of the function b along the event defined by d (a tube d_{TUBE} for pixelated scintillators and a LOR d_n for the continuous case) (Reader *et al* 2002). These line-function intersection methods can be justified on the basis of our method (defined by (19) and (21)). If the intrinsic uncertainty associated with the detection system is not considered then the probability $p(\mathbf{r}, d)$ in (24) is zero everywhere except at the points of the event d. Moreover, the probability of all points $\mathbf{r}_0$ along the LOR is constant and, therefore, the probability can go out of the integral, yielding that the probability of detection of a pair of photons emitted in a basis function b in d is proportional to the integral of the basis function along the event (tube or line) d.

4. Validation

The analytical methods that have been developed in sections 3.1 and 3.2 to compute the normalizing term and the system matrix have been implemented and subsequently evaluated. The well-known Monte Carlo simulator GATE (the Geant4 applications for emission tomography) (Jan *et al* 2004) has been used to validate our mathematical model and its implementation. In addition to the algorithm validation, some conclusions and contributions obtained after the algorithm implementation are pointed out in sections 4.1.1 and 4.2.1.
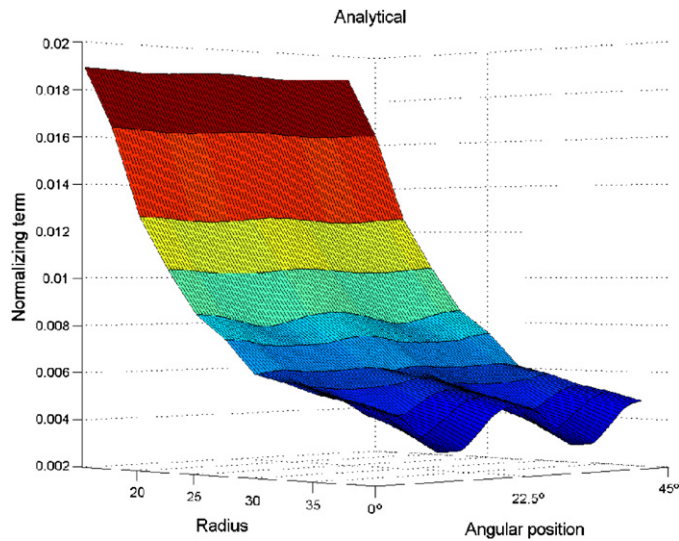
Figure 6. Normalizing term along sectors of 45° of circumferences of different radius in the central transaxial plane (xy). The radius is given in millimeters.

(This figure is in colour only in the electronic version)

4.1. Validation of the normalizing term

For the validation of the normalizing term, the proposed analytical scheme has been adapted for the experimental small animal PET described in Gimenez *et al* (2004). This PET scanner consists of two continuous lutetium oxyorthosilicate (LSO) detector heads. The dimensions of the setup (as defined in figure 1) are $W = 42$ mm, $L = 42$ mm, $H = 10$ mm and $S = 82$ mm, and the angular step of rotation around the z-axis is 22.5°.

The normalizing terms along the points of a circumference in the central transaxial plane (plane xy) placed in the center of the scanner and for a grid of points in the yz plane have been computed. For both experiments, the normalized mean-square error, NMSE (defined as $\text{NMSE} = \frac{1}{N} \sum_{i=0}^{i=N-1} [(X_{\text{an}_i} - X_{\text{MC}_i})^2 / \bar{X}_{\text{an}} \bar{X}_{\text{MC}}]$, where X_{an} contains the points obtained by our analytical method, X_{MC} contains the points obtained by the Monte Carlo simulator, N is the total number of computed points (i.e. the size of X_{an} and X_{MC}) and $\bar{X}_{\text{an}}$ and $\bar{X}_{\text{MC}}$ are the means of X_{an} and X_{MC}) is in the order of 10^{-3}. With regard to the computational time, for the yx plane simulations, one million gamma-pair emissions from 120 different point sources have been simulated using the Monte Carlo method. The execution time was around 500 h. The results achieved by means of the analytical method have been obtained in less than 40 s on the same computer.

4.1.1. Cylindrical symmetry.

One of the features that all the previous analytical implementations of the normalizing term share is the assumption of cylindrical symmetry with respect to the rotation axis (the z-axis in the scheme shown in figure 1). Figure 6 plots the normalizing term computed by means of the proposed analytical method along 45° (note that given the scanner rotation symmetry, the normalizing term must be periodic with a periodicity no greater than 22.5°) of different radius circumferences in the central transaxial plane centered in the z-axis. A simple look at this plot shows that the normalizing term along

a circumference centered in this axis is not a constant, and therefore it can be concluded that the cylindrical symmetry condition is not always fulfilled. To better illustrate this fact, the percentages of variation (computed as the ratio of the peak-to-peak difference to the mean value) of the normalizing term along some of these circumferences have been computed, and it has been seen that the larger radius circumferences show fluctuations that reach 40% of variation.

The periodical behavior that can be observed in figure 6 is caused by the rotation step of the scanner (the angular distance between two consecutive peaks corresponds to the rotation angular step). This means that the cylindrical symmetry assumption is appropriate for the case of scanners with continuous rotation around the z-axis, and it is even reasonable for the case of stepped rotation in very small angular steps. However, as the angular rotation step gets larger, this assumption can give rise to important inaccuracies in the computation of the normalizing term. This statement can be corroborated through a set of simulations for one of the commercially available small animal PET systems, the YAP-PET (Guerra *et al* 2000). The YAP-PET is a rotating planar detector PET scanner whose computer controlled rotation allows us to perform rotation angular steps of 0.7, 1.4, 2.8, 5.6, 11.2, 22.5, 45 and 90°. Figure 7 shows, for several of these rotation configurations, the values of fluctuation of the normalizing term (computed by means of the analytical method proposed here) along a circumference in the central transaxial plane as a function of its radius. As has been pointed out before, the percentage of variation gets more and more important as the rotation angle increases, reaching values of more than 300% in the 90° case.

4.2. Validation of the system matrix

For the continuous scintillator case, the experimental scheme proposed by Gimenez *et al* (2004) ($W = 42$ mm, $L = 42$ mm, $H = 10$ mm and $d = 82$ mm) has been implemented. For the pixelated case, a discretized version of the continuous setup has been chosen to perform the system matrix validation. The 42 mm $\times$ 42 mm detector heads have been divided into square detector elements of size $C = 6$ mm (the factor somewhat higher compared to reality).

Regarding the uncertainty estimation, as has been pointed out, the detector readout and signal processing involved in the event positioning depend strongly on each scanner design. Therefore, in order to perform high-quality reconstructions, the value of the Gaussian standard deviation (σ) that estimates the positioning error should be directly obtained from the scanner for which the system matrix is going to be computed. In this paper, for demonstration purposes, the value of σ has been computed by means of the Monte Carlo simulator. Nevertheless, the procedure to experimentally estimate the value of this parameter is similar to that followed in the Monte Carlo simulations: a narrow 511 keV gamma-ray beam must be generated normally incident on the center ($x = 0, z = 0$) of the detection module. A ^{22}Na point source with electronic collimation and a precision X–Y stage can be used to perform the experiment. List-mode data must be generated to give the (x, y, z) location of each detection. Then, for each uncertainty direction, (x and z), the sample standard deviation can be estimated by applying the following expression:

$$\sigma_k = \sqrt{\frac{1}{N-1} \sum_{i=1}^{N} (k_i - \mu_k)^2}, k = x, z, \tag{25}$$

where $\{k_1, k_2, \ldots, k_N\}$ is the sample of detected positions in each direction, and μ_k is the mean of each sample, which should match the detector center ($\mu_x = \mu_z = 0$) in this case.

In order to estimate the dependence of σ with the DOI (see section 3.2.2), the experiment must be carried out with different thickness scintillators. For each thickness, it will be
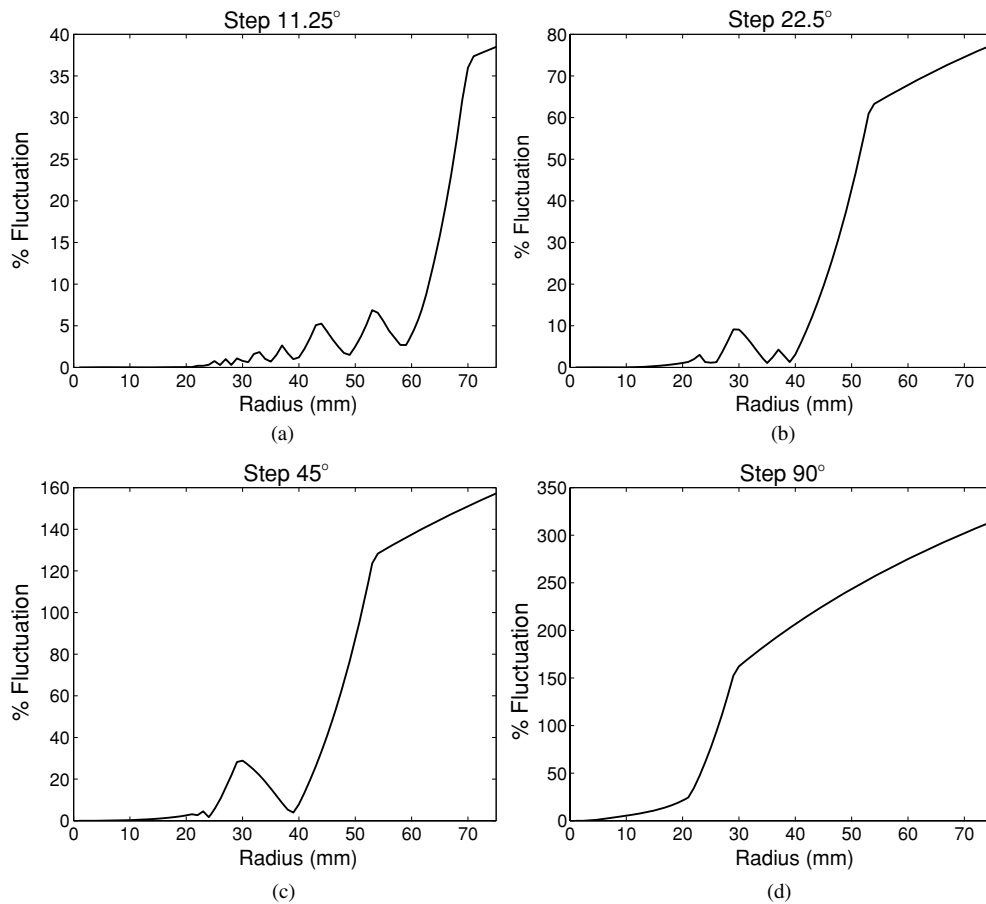
Figure 7. Fluctuation of the normalizing term (computed as the ratio of the peak-to-peak difference to the mean value) along a circumference as a function of its radius for the different rotation configurations (rotation angular steps of 11.2 (c), 22.5 (d), 45 (e) and 90° (f)) of the YAP-PET scanner. The variation is negligible for the smallest rotation steps but can reach values of more than 300% for the 90° rotation case.

considered that the maximum positioning error is due to those photons that interact in the internal surface of the detector ($l = 0$). It will be therefore assumed that the standard deviation obtained for a given thickness defines the detection uncertainty for a gamma photon seeing that crystal thickness after its first interaction. The parameters m and b that define (16) can be extracted by fitting the σ-thickness curves obtained to a linear polynomial.

The standard deviations σ have been estimated applying the described procedure to the two scanners (continuous and pixelated) for which the system matrix is going to be computed. One million normally incident emissions from a point source located at the center of the setup were simulated for five different detector thicknesses. The histograms for the z position detected are shown in figure 8 for both continuous and pixelated LSO detectors with a thickness of $H = 10$ mm. Figure 9 shows the standard deviation as a function of the crystal thickness for four different detector materials. These graphs provide a visual demonstration of the statements made in section 3.2.2; the detection uncertainty can be fitted to a Gaussian profile and the dependence of σ with the thickness can be approximated by a linear function.
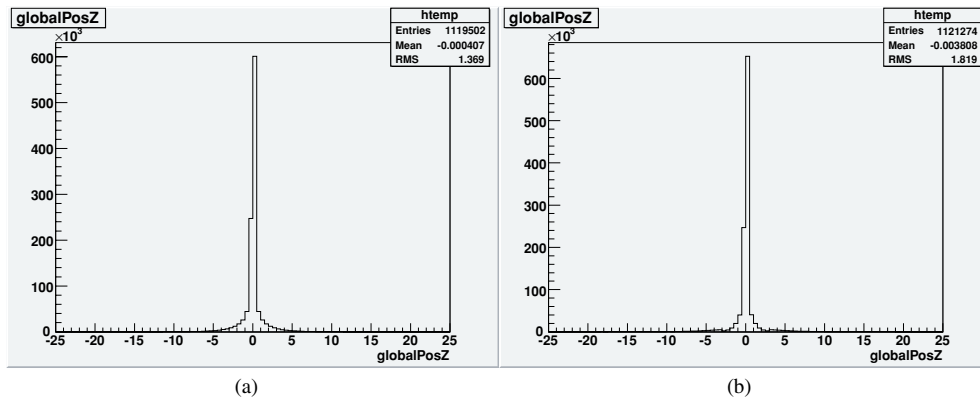
Figure 8. Histograms of the *z* position detected after one million normally incident emissions from a point source positioned at $(0, 0, 0)$: histogram for a continuous detector of thickness $H = 10$ mm (a), and histogram for a pixelated detector of thickness $H = 5$ mm (b).
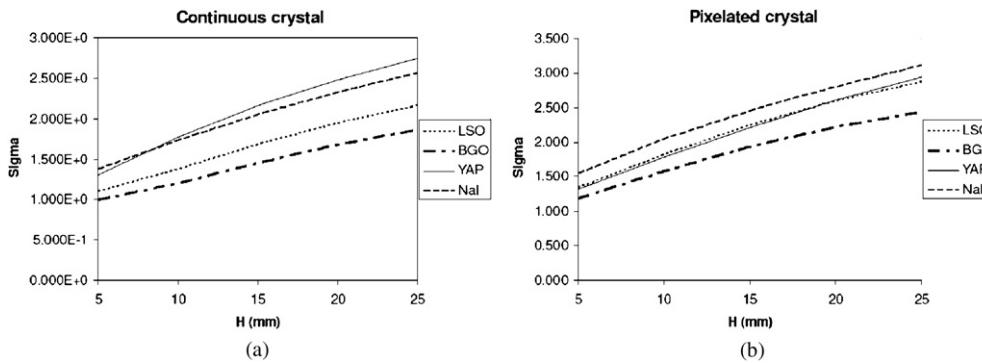
Figure 9. Standard deviation as a function of the crystal thickness for four different crystal materials.

Once the σ-thickness dependence has been estimated, the system matrix for a grid of points in the yz plane has been calculated for two different lines of response (oblique and perpendicular to the detector planes) and compared with the Monte Carlo results. The first line of response, perpendicular to the detector planes, is defined by the detection coordinates (in millimeters): $(0, -41, 0)$ and $(0, 41, 0)$, and the second one, oblique, by: $(12, -41, 12)$ and $(-12, 41, -12)$. In all cases, the NMSE is in the order of 10^{-2}. Regarding the computational cost, for each of the lines of response the grid of points in the yz plane was composed of 120 point sources. With regard to the Monte Carlo method, ten million gamma-pair emissions for 20 different point sources (just the sources in $z = 0$ had to be computed as the rest were obtained by moving the reference LOR with respect to this axis) have been simulated. The execution time was 80 h. Simulations with the analytical approach have been obtained in less than 2 min for each line.

4.2.1. Contributions. Table 1 summarizes the improvement achieved, in terms of NMSE, with respect to the Monte Carlo simulations. For both continuous and pixelated scintillators, the column labeled 'Analytical' contains the NMSE obtained with the method introduced in

Table 1. Quantification, in terms of the NMSE with respect to the Monte Carlo results of the improvement obtained by means of the addition of the uniform distribution term, the exponential model for the probability of interaction through the crystal and the DOI variability of the uncertainty.

	NMSE			
	Continuous scintillator			
	Analytical	No $\cos\varphi$	Uniform	Constant-sigma
Perpendicular	0.05	4.50	0.69	0.15
Oblique	0.05	3.83	0.79	0.13
	Pixelated scintillator			
	Analytical	No $\cos\varphi$	Uniform	Constant-sigma
Perpendicular	0.03	4.56	0.68	0.11
Oblique	0.08	4.92	1.10	0.18

this paper, the column 'No $\cos\varphi$' contains the NMSE obtained without introducing the term for the uniform distribution of the LORS; 'Uniform' contains the results with an uniform model for the probability of interaction through the crystal and 'Fixed sigma' contains the error for the results with a constant value of sigma. The value of the fixed sigma has been chosen to be the maximum standard deviation σ_H (given by the evaluation of (16) in $t(l = 0) = H$).

5. Discussion

We have developed analytical methods to compute both the normalizing and the system matrix terms for the EM-ML based algorithms that are based strictly on their statistical definitions and that are valid for the continuous detector case. Our development comprises two well-differentiated steps. First, the normalizing term and the system matrix for a single emitting point are computed. It is in this first step that the geometry of the planar detector scanner, the uniform distribution of emitted lines in the sphere, the DOI of the incident gamma rays, the efficiency of the scintillators, the interactions of the gamma rays with matter, and the intrinsic resolution of the readout and signal processing are taken into account. Moreover, the method can be easily expanded to take into account further refinements in the image formation process in PET. In the second step, the results for a single emitting point are extended to the case of an arbitrary basis function as long as it can be reduced to a probability density function. This conversion from a point to a basis function explicitly relates the continuous quantity that we want to measure (concentration of tracer distribution) with its discrete representation without the heuristic approximations made by other methods.

Within the limitations of the Monte Carlo simulations, the new analytical method provides similar results at a small fraction of the computational cost. Therefore, it is a convenient framework to model the PET process and to quantify the significance of different physical factors that take place in it. In this regard, the method developed could be thought of as an excellent tool for the design and evaluation of PET cameras.

In addition to the already-cited properties, the new developed method for the computation of the normalizing and system matrix terms deviates from previous works in that:

(i) It can use directly list-mode data produced by continuous detectors. That is, no data rebinning is needed. Therefore, all the information contained in the raw data is accessible to the reconstruction method.

(ii) Regarding the normalizing term, it does not assume cylindrical symmetry. All the alternative analytical calculations of point sensitivity valid for the case of continuous

detectors assume cylindrical symmetry. Nevertheless, the results obtained by our method show that dual-head PET cameras do not always present exact cylindrical symmetry.

(iii) Regarding the system matrix, it explicitly takes into account the uniform distribution of emitted lines in the sphere, it assumes an exponential model for the probability of detection along the photon path and it models the dependence or the uncertainty in the detection with the depth of the first interaction.

Acknowledgments

Appendix A.

A.1. Derivation of the terms $\alpha_\varphi(\mathbf{r}_0, \gamma)$ and $\beta_\varphi(\mathbf{r}_0, \gamma)$

In this section, we provide an analytical derivation of the terms $\alpha_\varphi(\mathbf{r}_0, \gamma)$ and $\beta_\varphi(\mathbf{r}_0, \gamma)$ used in section 3.1.

The angles of view from the point $\mathbf{r}_0$ of coordinates (x_0, y_0, z_0) into each detector within the plane Π_γ (see figure A1) are

$$\alpha_{\varphi 1}(\mathbf{r}_0, \gamma) = \angle(D\mathbf{r}_0 F) \tag{A.1a}$$

$$\beta_{\varphi 1}(\mathbf{r}_0, \gamma) = \angle(F\mathbf{r}_0 C) \tag{A.1b}$$

$$\alpha_{\varphi 2}(\mathbf{r}_0, \gamma) = \angle(E\mathbf{r}_0 B) \tag{A.1c}$$

$$\beta_{\varphi 2}(\mathbf{r}_0, \gamma) = \angle(A\mathbf{r}_0 E). \tag{A.1d}$$

The analytical expressions for the points A, B, C, D, E and F are

$$A = \left(x_0 - \left(\frac{S}{2} + y_0\right)\tan\gamma, -\frac{S}{2}, \frac{W}{2}\right) \tag{A.2a}$$

$$B = \left(x_0 - \left(\frac{S}{2} + y_0\right)\tan\gamma, -\frac{S}{2}, -\frac{W}{2}\right) \tag{A.2b}$$

$$C = \left(x_0 + \left(\frac{S}{2} - y_0\right)\tan\gamma, \frac{S}{2}, -\frac{W}{2}\right) \tag{A.2c}$$

$$D = \left(x_0 + \left(\frac{S}{2} - y_0\right)\tan\gamma, \frac{S}{2}, \frac{W}{2}\right) \tag{A.2d}$$

$$E = \left(x_0 - \left(\frac{S}{2} + y_0\right)\tan\gamma, -\frac{S}{2}, z_0\right) \tag{A.2e}$$

$$F = \left(x_0 + \left(\frac{S}{2} - y_0\right)\tan\gamma, \frac{S}{2}, z_0\right). \tag{A.2f}$$
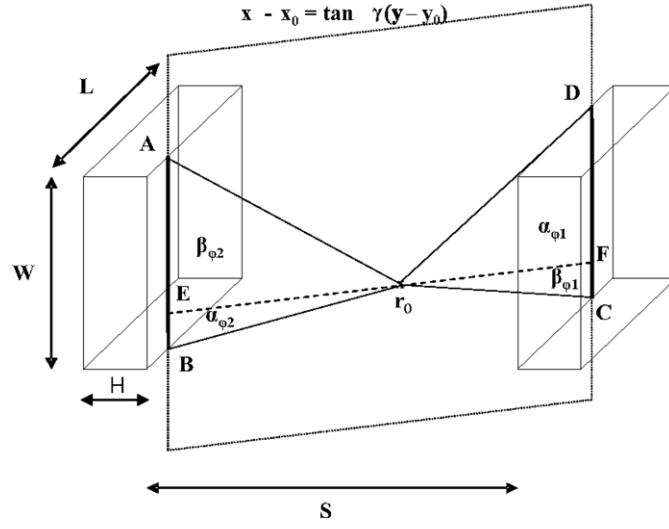
Figure A1. Geometrical characterization of the range of angles of view from the point $\mathbf{r}_0$ into the detector heads within the plane Π_γ.

The total area of detectable lines emitted by $\mathbf{r}_0$ in the plane Π_γ is limited by $\alpha_\varphi(\mathbf{r}_0, \gamma)$ and $\beta_\varphi(\mathbf{r}_0, \gamma)$:

$$\alpha_\varphi(\mathbf{r}_0, \gamma) = \min(\alpha_{\varphi1}(\mathbf{r}_0, \gamma), \alpha_{\varphi2}(\mathbf{r}_0, \gamma)) \tag{A.3a}$$

$$\beta_\varphi(\mathbf{r}_0, \gamma) = \min(\beta_{\varphi1}(\mathbf{r}_0, \gamma), \beta_{\varphi2}(\mathbf{r}_0, \gamma)). \tag{A.3b}$$

A.2. Derivation of the terms $\alpha_\gamma(\mathbf{r}_0)$ and $\beta_\gamma(\mathbf{r}_0)$

In this section, we provide an analytical derivation of the terms $\alpha_\gamma(\mathbf{r}_0)$ and $\beta(\mathbf{r}_0)$ used in section 3.1.

The expressions for the angle values seen by the point $\mathbf{r}_0$ in the XY plane (as shown in figure A2) are

$$\alpha_{\gamma1}(\mathbf{r}_0) = \arctan\left(\frac{\frac{L}{2} + x_0}{\frac{S}{2} - y_0}\right) \tag{A.4a}$$

$$\beta_{\gamma1}(\mathbf{r}_0) = \arctan\left(\frac{\frac{L}{2} - x_0}{\frac{S}{2} - y_0}\right) \tag{A.4b}$$

for the right side detector, and

$$\alpha_{\gamma2}(\mathbf{r}_0) = \arctan\left(\frac{\frac{L}{2} - x_0}{\frac{S}{2} + y_0}\right) \tag{A.5a}$$

$$\beta_{\gamma2}(\mathbf{r}_0) = \arctan\left(\frac{\frac{L}{2} + x_0}{\frac{S}{2} + y_0}\right) \tag{A.5b}$$
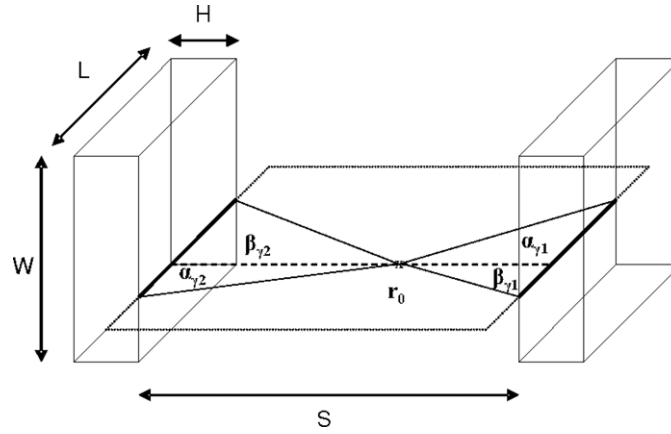
Figure A2. Geometrical characterization of the range of angles of view from the point $\mathbf{r}_0$ into the detector heads within the plane XY.

for the left side detector.

The total area of detectable lines emitted by $\mathbf{r}_0$ in the plane XY_γ is limited by $\alpha_\gamma(\mathbf{r}_0)$ and $\beta_\gamma(\mathbf{r}_0)$:

$$\alpha_\gamma(\mathbf{r}_0) = \min(\alpha_{\gamma 1}(\mathbf{r}_0), \alpha_{\gamma 2}(\mathbf{r}_0)), \tag{A.6a}$$

$$\beta_\gamma(\mathbf{r}_0) = \min(\beta_{\gamma 1}(\mathbf{r}_0), \beta_{\gamma 2}(\mathbf{r}_0)). \tag{A.6b}$$

A.3. Intersection points

In this section, we provide expressions for the intersection points $\mathbf{p}'_1(x'_1, y'_1, z'_1)$ and $\mathbf{p}'_2(x'_2, y'_2, z'_2)$ mentioned in section 3.2. As has been previously noted $\mathbf{p}'_1$ and $\mathbf{p}'_2$ correspond to the two points defining the line d'_{LOR} at which the event actually took place instead of in the detected LOR (defined by the positions $\mathbf{p}_1$ and $\mathbf{p}_2$). As uncertainty is considered just in the X and Z directions, it follows that

$$y'_1 = y_1, \tag{A.7a}$$

$$y'_2 = y_2. \tag{A.7b}$$

Integration variables $z'_1(\mathbf{r}_0, \varphi)$ and $z'_2(\mathbf{r}_0, \varphi)$ are the z positions of the d'_{LOR} ends in the left and right detectors (planes $y = y_1$ and $y = y_2$, respectively), as a function of the inclination angle with respect to $z = z_0$. The expression for this variable in terms of $\mathbf{r}_0$ position is

$$z'_1(\mathbf{r}_0, \varphi) = z_0 + d(\mathbf{r}_0, E) \tan\varphi \tag{A.8a}$$

$$z'_2(\mathbf{r}_0, \varphi) = z_0 - d(\mathbf{r}_0, F) \tan\varphi. \tag{A.8b}$$

As $\mathbf{r}_0$, F and E all belong to the plane $z = z_0$, distances between them are

$$d(\mathbf{r}_0, E) = \sqrt{(x_0 - x_1)^2 + (y_0 - y_1)^2}, \tag{A.9a}$$

$$d(\mathbf{r}_0, F) = \sqrt{(x_0 - x_2)^2 + (y_0 - y_2)^2}. \tag{A.9b}$$

Expressions for E and F have already been developed to compute the integration limits. Integration variables $x'_1(\mathbf{r}_0, \gamma)$ and $x'_2(\mathbf{r}_0, \gamma)$ turn out to be

$$x'_1(\mathbf{r}_0, \gamma) = x_0 + d(\mathbf{r}_0, E') \tan \gamma, \tag{A.10a}$$

$$x'_2(\mathbf{r}_0, \gamma) = x_0 - d(\mathbf{r}_0, F') \tan \gamma. \tag{A.10b}$$

Finally, distances from E' and F' to $\mathbf{r}_0$ are

$$d(\mathbf{r}_0, E') = \sqrt{(z_0 - z'_1)^2 + (y_0 - y'_1)^2}, \tag{A.11a}$$

$$d(\mathbf{r}_0, F') = \sqrt{(z_0 -' z_2)^2 + (y_0 - y'_2)^2}. \tag{A.11b}$$

Expressions for E' and F' have been computed to obtain the integration limits.

A.4. Crystal thickness after first photon interaction

As shown in figure 5, in (16), $t(l)$ is the crystal thickness that the photon 'sees' after an interaction at l units of crystal in the d'_{LOR} direction (i.e., the direction defined by the point $\mathbf{r}_0$ and the angles γ, φ). The value of $t(l)$ is given by

$$t(l) = \frac{H}{2} - |(l \cos \varphi \cos \gamma)|. \tag{A.12}$$

A.5. Integration limits

In this section, we provide closed form expressions for the integration limits $\varphi_{\min}, \varphi_{\max}, \gamma_{\min}$, $\gamma_{\max}$ used in section 3.2.3.

In a similar way to what has been done in the previous section for the normalizing term, the integration limits $\varphi_{\min}$, $\varphi_{\max}$ and $\gamma_{\min}$, $\gamma_{\max}$ can be calculated as the angles of view from the point $\mathbf{r}_0$ into the detector heads in the plane Π_γ (axial uncertainty) and in the plane Π_φ (tangential uncertainty), respectively (see figures 3 and 4 for the continuous case). But now, as mentioned in section 3.2, the limits are restricted by the resolution of the scintillator. This restriction corresponds in each direction of uncertainty to the minimum of three times the maximum standard deviation ($\sigma(l = 0)$) from the detected points and the detector limits. The expression and methodology needed to compute the maximum standard deviation ($\sigma(l = 0)$) have been provided in section 4.

Let us consider first the uncertainty in the axial direction. For the continuous scintillator situation, the limits imposed by three times the standard deviation from the detected points $\mathbf{p}_1(x_1, y_1, z_1)$ and $\mathbf{p}_2(x_2, y_2, z_2)$ in this direction are given by the points A, B, C, D (see figure A3):

$$A = \left(x_1, y_1, \min\left(z_1 + 3\sigma_z(l = 0), \frac{W}{2}\right)\right) \tag{A.13a}$$

$$B = \left(x_1, y_1, \max\left(z_1 - 3\sigma_z(l = 0), -\frac{W}{2}\right)\right) \tag{A.13b}$$

$$C = \left(x_2, y_2, \max\left(z_2 - 3\sigma_z(l = 0), -\frac{W}{2}\right)\right) \tag{A.13c}$$

$$D = \left(x_2, y_2, \min\left(z_2 + 3\sigma_z(l = 0), \frac{W}{2}\right)\right). \tag{A.13d}$$
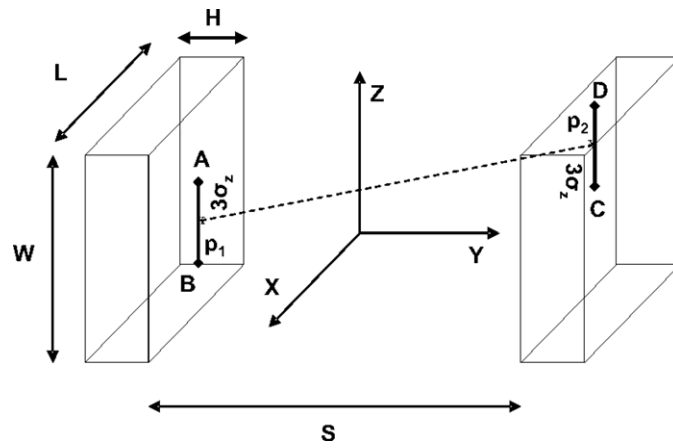
Figure A3. A, B, C and D are the points located at three times the standard deviation in the axial direction from the detected points $\mathbf{p}_1$ and $\mathbf{p}_2$.
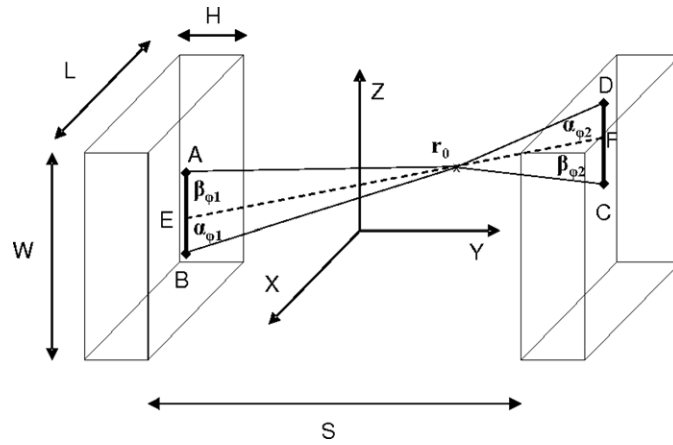
Figure A4. Angles of view from $\mathbf{r}_0$ within the Gaussian limits and plane Π_γ.

The angles seen by $\mathbf{r_0}$ into the detector heads restricted to these limits are (see figure A4)

$$\alpha_{\varphi 1} = \angle(B\mathbf{r}_0 E) \tag{A.14a}$$

$$\beta_{\varphi 1} = \angle(A\mathbf{r}_0 E) \tag{A.14b}$$

$$\alpha_{\varphi 2} = \angle(D\mathbf{r}_0 F) \tag{A.14c}$$

$$\beta_{\varphi 2} = \angle(C\mathbf{r}_0 F). \tag{A.14d}$$

Points E and F are the ends of the segment resulting from the intersection of the plane $z = z_0$ with the rectangle given by $ABCD$. The analytical expressions (valid for both the continuous and pixelated detector cases) for E and F are

$$E = (x_1, y_1, z_0) \tag{A.15a}$$
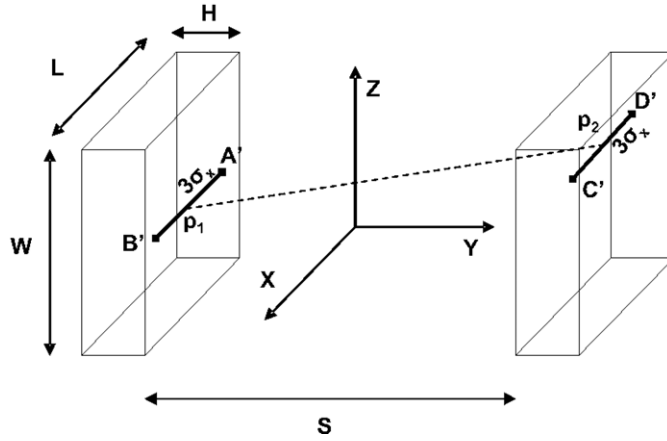
Figure A5. A', B', C' and D' are the points located at three times the standard deviation in the tangential direction from the detected points $\mathbf{p}_1$ and $\mathbf{p}_2$.

$$F = (x_2, y_2, z_0). \tag{A.15b}$$

Finally, integration angles α_φ, β_φ in the axial direction will be given by

$$\alpha_\varphi = \min(\alpha_{\varphi 1}, \alpha_{\varphi 2}) \tag{A.16a}$$

$$\beta_\varphi = \min(\beta_{\varphi 1}, \beta_{\varphi 2}). \tag{A.16b}$$

Similar reasoning follows for the computation of the limits regarding the tangential uncertainty. Therefore, for the continuous detector case, the limits imposed by three times the standard deviation are given by points A', B', C', D' (see figure A5):

$$A' = \left(\max\left(x_1 - 3\sigma_x(l = 0), -\frac{L}{2} \right), y_1, z_1 \right) \tag{A.17a}$$

$$B' = \left(\min\left(x_1 + 3\sigma_x(l = 0), \frac{L}{2} \right), y_1, z_1 \right) \tag{A.17b}$$

$$C' = \left(\min\left(x_2 + 3\sigma_x(l = 0), \frac{L}{2} \right), y_2, z_2 \right) \tag{A.17c}$$

$$D' = \left(\max\left(x_2 - 3\sigma_x(l = 0), -\frac{L}{2} \right), y_2, z_2 \right). \tag{A.17d}$$

The angles of view from $\mathbf{r}_0$ into detector heads within these limits, for both pixelated and continuous detectors are (see figure A6)

$$\alpha_{\gamma 1} = \angle E' \mathbf{r}_0 B' \tag{A.18a}$$

$$\beta \gamma_1 = \angle A' \mathbf{r}_0 E' \tag{A.18b}$$

$$\alpha_{\gamma 2} = \angle D' \mathbf{r}_0 F' \tag{A.18c}$$
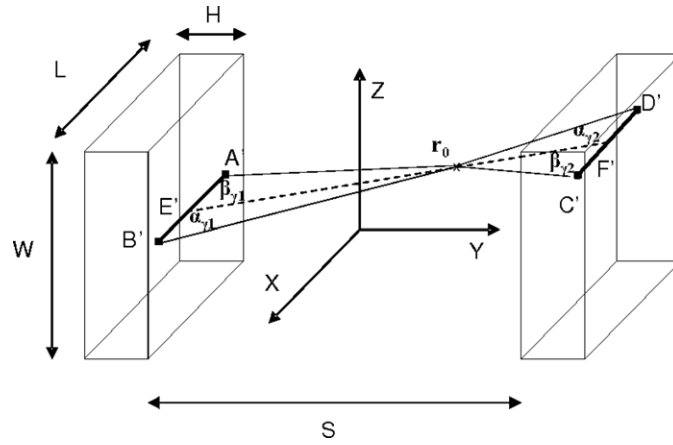
Figure A6. Angles of view from $\mathbf{r}_0$ within the Gaussian limits in the plane Π_φ.

$$\beta_{\gamma 2} = \angle C' \mathbf{r}_0 F', \tag{A.18d}$$

where E' and F' are the ends of the intersection of the plane $x = x_0$ with the rectangle given by $A'B'C'D'$:

$$E' = (x_0, y_1, z_1) \tag{A.19a}$$

$$F' = (x_0, y_2, z_2). \tag{A.19b}$$

Integration limits in the tangential direction are

$$\alpha_\gamma = \min(\alpha_{\gamma 1}, \alpha_{\gamma 2}) \tag{A.20a}$$

$$\beta_\gamma = \min(\beta_{\gamma 1}, \beta_{\gamma 2}). \tag{A.20b}$$

A.6. Development of $p(\mathbf{r_0}, d_{\text{tube}})$ and $p(\mathbf{r_0}, d_n)$

Substituting in (19) the value of $f(\mathbf{r}_0, d_{\text{LOR}})$ by the expression given by (18), and then replacing the value of $f(d_{\text{LOR}}|d'_{\text{LOR}})_{\text{DOI}}$ by the expression in (17) and rearranging terms leads to

$$p(\mathbf{r}_0, d_{\text{tube}}) = \int_{\alpha_\gamma(3\sigma_H, L)}^{\beta_\gamma(3\sigma_H, L)} \int_{\alpha_\varphi(3\sigma_H, W)}^{\beta_\varphi(3\sigma_H, W)} \left\{ \int_0^{L_1(\mathbf{r}_0, \varphi, \gamma)} [p_1(\mathbf{r}_0, \gamma, \varphi, l_1) f(l_1)] \, dl_1 \right.$$
$$\left. \int_0^{L_2(\mathbf{r}_0, \varphi, \gamma)} [p_2(\mathbf{r}_0, \gamma, \varphi, l_2) f(l_2)] \, dl_2 \right\} \frac{\cos\varphi}{2\pi} \, d\varphi \, d\gamma, \tag{A.21}$$

where

$$p_1(\mathbf{r}_0, \gamma, \varphi, l_1) = p(C_{1x}|x'_1(\mathbf{r}_0, \gamma, l_1)) p(C_{1z}|z'_1(\mathbf{r}_0, \varphi, l_1)) \tag{A.22}$$

$$p_2(\mathbf{r}_0, \gamma, \varphi, l_2) = p(C_{2x}|x'_2(\mathbf{r}_0, \gamma, l_2)) p(C_{2z}|z'_2(\mathbf{r}_0, \varphi, l_2)) \tag{A.23}$$

and

$$p(C_{1x}|x_1'(\mathbf{r}_0, \gamma, l_1)) = \frac{1}{\sqrt{2\pi}\sigma(l)} \int_{C_{1x}} e^{-\frac{1}{2\sigma(l)^2}(x_1'(\mathbf{r}_0,\gamma,l_1)-x_1)^2} \, dx_1 \qquad (A.24a)$$

$$p(C_{1z}|z_1'(\mathbf{r}_0, \varphi, l_!)) = \frac{1}{\sqrt{2\pi}\sigma(l)} \int_{C_{1z}} e^{-\frac{1}{2\sigma(l)^2}(z_1'(\mathbf{r}_0,\varphi,l_1)-z_1)^2} \, dz_1 \qquad (A.24b)$$

$$p(C_{2x}|x_2'(\mathbf{r}_0, \gamma, l_2)) = \frac{1}{\sqrt{2\pi}\sigma(l)} \int_{C_{2x}} e^{-\frac{1}{2\sigma(l)^2}(x_2'(\mathbf{r}_0,\gamma,l_2)-x_2)^2} \, dx_2 \qquad (A.24c)$$

$$p(C_{2z}|z_2'(\mathbf{r}_0, \varphi, l_2)) = \frac{1}{\sqrt{2\pi}\sigma(l)} \int_{C_{2z}} e^{-\frac{1}{2\sigma(l)^2}(z_2'(\mathbf{r}_0,\varphi,l_2)-z_2)^2} \, dz_2. \qquad (A.24d)$$

The integrals in (A.24) can be analytically solved. Replacing in each of these four expressions $\frac{1}{\sqrt{2}\sigma(l)}(x_i - x_i'(\mathbf{r}_0, \gamma, l))i = 1, 2$ and $\frac{1}{\sqrt{2}\sigma(l)}(z_i - z_i'(\mathbf{r}_0, \varphi, l))i = 1, 2$ by u we obtain the following:

$$p(C_{1x}, x_1'(\mathbf{r}_0, \gamma, l_1)) = \frac{1}{\sqrt{\pi}} \int_{C_{1xu}} e^{-u^2} \, du \qquad (A.25a)$$

$$p(C_{1z}, z_1'(\mathbf{r}_0, \varphi, l_1)) = \frac{1}{\sqrt{\pi}} \int_{C_{1zu}} e^{-u^2} \, du \qquad (A.25b)$$

$$p(C_{2x}, x_2'(\mathbf{r}_0, \gamma, l_2)) = \frac{1}{\sqrt{\pi}} \int_{C_{2xu}} e^{-u^2} \, du \qquad (A.25c)$$

$$p(C_{2z}, z_2'(\mathbf{r}_0, \varphi, l_2)) = \frac{1}{\sqrt{\pi}} \int_{C_{2zu}} e^{-u^2} \, du, \qquad (A.25d)$$

and the integration limits become

$$C_{1x} = \left[\frac{1}{\sqrt{2}\sigma(l)}(C_{1xl} - x_1'), \frac{1}{\sqrt{2}\sigma(l)}(C_{1xh} - x_1') \right] \qquad (A.26a)$$

$$C_{1z} = \left[\frac{1}{\sqrt{2}\sigma(l)}(C_{1zl} - z_1'), \frac{1}{\sqrt{2}\sigma(l)}(C_{1zh}) - z_1' \right] \qquad (A.26b)$$

$$C_{2x} = \left[\frac{1}{\sqrt{2}\sigma(l)}(C_{2xl} - x_2'), \frac{1}{\sqrt{2}\sigma(l)}(C_{2zh} - x_2') \right] \qquad (A.26c)$$

$$C_{2z} = \left[\frac{1}{\sqrt{2}\sigma(l)}(C_{2zl} - z_2'), \frac{1}{\sqrt{2}\sigma(l)}(C_{2zh} - z_2') \right]. \qquad (A.26d)$$

The integrals in (A.26) can be analytically expressed as a function of the erf function $\mathrm{erf}(z) = \frac{1}{\sqrt{\pi}} \int_0^z e^{-t^2} \, dt$:

$$p(C_{1x}, x_1'(\mathbf{r}_0, \gamma, l_1)) = \mathrm{erf}\left(\frac{1}{\sqrt{2}\sigma(l)}(C_{1xl} - x_1') \right) - \mathrm{erf}\left(\frac{1}{\sqrt{2}\sigma(l)}(C_{1xh} - x_1') \right) \qquad (A.27a)$$

$$p(C_{1z}, z_1'(\mathbf{r}_0, \varphi, l_!)) = \mathrm{erf}\left(\frac{1}{\sqrt{2}\sigma(l)}(C_{1zl} - z_1') \right) - \mathrm{erf}\left(\frac{1}{\sqrt{2}\sigma(l)}(C_{1zh} - z_1') \right) \qquad (A.27b)$$

$$p(C_{2x}, x_2'(\mathbf{r}_0, \gamma, l_2)) = \mathrm{erf}\left(\frac{1}{\sqrt{2}\sigma(l)}(C_{2xl} - x_2') \right) - \mathrm{erf}\left(\frac{1}{\sqrt{2}\sigma(l)}(C_{2xh} - x_2') \right) \qquad (A.27c)$$

$$p(C_{2z}, z_2'(\mathbf{r}_0, \varphi, l_2)) = \mathrm{erf}\left(\frac{1}{\sqrt{2}\sigma(l)}(C_{2zl} - z_2') \right) - \mathrm{erf}\left(\frac{1}{\sqrt{2}\sigma(l)}(C_{2zh} - z_2') \right). \qquad (A.27d)$$

References

Giménez E N *et al* 2004 Detector optimization of a small animal PET camera based on continuous LSO crystals and flat panel PS-PMTs *Proc. IEEE Nuclear Science Symp.* vol 6 pp 3885–9

Guerra A D, Damiani C, Domenico G D, Motta A, Giganti M, Marchesini R, Piffanelli A, Sabba N, Sartori L and Zavattini G 2000 An integrated PET-SPECT small animal imager: preliminary results *IEEE Trans. Nucl. Sci.* **47** 1537–40

Jan S *et al* 2004 GATE: a simulation toolkit for PET and SPECT *Phys. Med. Biol.* **49** 4543–61

Levkovtiz R, Falikman D, Zibulevsky M, Ben-Tal A and Nemirovski A 2001 The design and implementation of COSEM, an iterative algorithm for fully 3-D listmode data *IEEE Trans. Med. Imaging* **20** 633–42

Lewitt R M and Matej S 2003 Overview of methods for image reconstruction from projections in emission computed tomography *Proc. IEEE* **91** 1588–611

Ortuño J E, Guerra-Gutierrez P, Rubio J L, Kontaxakis G and Santos A 2006 3D-OSEM iterative image reconstruction for high-resolution PET using precalculated system matrix *Nucl. Instrum. Methods* A **569** 440–4

Ortuño J E, Kontaxakis G, Guerra P and Santos A 2004 3D-OSEM Transition matrix for high resolution PET imaging with modeling of the gamma-event detection *Proc. IEEE Medical Imaging Conf. (Rome, Italy)* vol M5–206 pp 168–72 (in CD-ROM)

Parra L and Barrett H H 1998 List-mode likelihood: EM algorithm and image quality estimation demonstrated on 2-D PET *IEEE Trans. Med. Imaging* **17** 228–35

Phelps M E and Cherry S R 1998 The changing design of positron imaging systems *Clin. Positron Imaging* **1** 31–45

Qi J, Leahy R M, Cherry S R, Chatziioannou A and Farquhar T H 1998 High-resolution 3D Bayesian image reconstruction using the microPET small-animal scanner *Phys. Med. Biol.* **43** 1001–13

Rahmim A, Cheng J C, Blinder S, Camborde M L and Sossi V 2005 Statistical dynamic image reconstruction in state-of-the-art high-resolution PET *Phys. Med. Biol.* **50** 4887–912

Reader A J, Erlandsson K, Flower M A and Ott R J 1998 Fast accurate iterative reconstruction for low-statistics positron volume imaging *Phys. Med. Biol.* **43** 835–46

Reader A J, Manavaki R, Zhao S, Julyan P J, Hastings D L and Zweit J 2002 Accelerated list-mode EM algorithm *IEEE Trans. Nucl. Sci.* **49** 42–9

Sanchez F, Benlloch J M, Escat B, Pavon N, Porras E, Kadi-Hanifi D, Ruiz J A, Mora F J and Sebastia A 2004 Design and tests of a portable mini gamma camera *Med. Phys.* **31** 1384–97

Scheins J J, Boschen F and Herzog H 2006 Analytical calculation of volumes-of-intersection for iterative, fully 3D PET reconstruction *IEEE Trans. Med. Imaging* 1363–9

Siegel S, Cherry S R, Ricci A R, Shao Y P and Phelps M E 1995 Development of continuous detectors for a high-resolution animal PET system *IEEE Trans. Nucl. Sci.* **42** 1069–74

Soares E J, Germino K W, Glick S J and Stodilka R Z 2003 Determination of three-dimensional voxel sensitivity for two- and three-header coincidence imaging *IEEE Trans. Nucl. Sci.* **50** 405–12

Staelens S, D'Asseler Y, Vandenberghe S, Koole M, Lemahieu I and Van de Walle R V 2004 A three-dimensional theoretical model incorporating spatial detection uncertainty in continuous detector PET *Phys. Med. Biol.* **49** 2337–50

Stickel J R and Cherry S R 2005 High-resolution PET detector design: modelling components of intrinsic spatial resolution *Phys. Med. Biol.* **50** 179–95

Tavernier S, Bruyndonckx P, Leonard S and Devroede O 2005 A high-resolution PET detector based on continuous scintillators *Nucl. Instrum. Methods* A **537** 321–5

Vardi Y, Shepp L A and Kaufman L 1985 A statistical-model for positron emission tomography *J. Am. Stat. Assoc.* **80** 8–20